Intrinsic and extrinsic relaxation mechanisms for controlling spin current intensity in Fe100– x Cox/Ta bilayers

D Velázquez Rodriguez, J E Gómez, L Avilés-Félix, J L Ampuero Torres, T E Torres, A A Pérez Martínez, L Morbidel, D Goijman, J C Rojas Sánchez, M H Aguirre, et al.

Published in Journal of Physics D: Applied Physics, vol. 57 art. 395003 (2024) http://dx.doi.org/10.1088/1361-6463/ad5b6d.

Intrinsic and extrinsic relaxation mechanisms for controlling spin current intensity in $Fe_{100-x}Co_x$/Ta bilayers

D. Velázquez Rodriguez[1,2], J. E. Gómez[1,2], L. Avilés-Félix[1,2,3], J. L. Ampuero Torres[1,2,3], T. E. Torres[1,2], A. A. Pérez Martínez[1,2,3], L. Morbidel[3], D. Goijman[1,2], J. C. Rojas Sánchez[4], M. H. Aguirre[5,6,7], J. Milano[1,2,3], A. Butera[1,2,3]

[1] Instituto de Nanociencia y Nanotecnología (CNEA - CONICET), Nodo Bariloche, Av. Bustillo 9500, (8400) Bariloche, Río Negro, Argentina

[2]Laboratorio Resonancias Magnéticas, Centro Atómico Bariloche, Av. Bustillo 9500, (8400) Bariloche (RN), Argentina

[3] Instituto Balseiro, Universidad Nacional de Cuyo (UNCuyo), Comisión Nacional de Energía Atómica (CNEA), R8402AGP San Carlos de Bariloche, Río Negro, Argentina

[4] Institut Jean Lamour, Université de Lorraine CNRS UMR 7198, Nancy, France

[5] Instituto de Nanociencia y Materiales de Aragón (INMA-CSIC), Campus Río Ebro, Universidad de Zaragoza, Spain

[6] Dpto. de Física de la Materia Condensada, Campus Río Ebro, Universidad de Zaragoza, Spain

[7] Laboratorio de Microscopías Avanzadas Edificio I+D, Campus Río Ebro, Universidad de Zaragoza, Spain

E-mail: daniel.velazquez@cab.cnea.gov.ar

August 2017

Abstract. Controlling the damping parameter in metallic ferromagnetic thin films is a key step for spintronic applications in which spin currents are generated by spin pumping. The coexistence of two states with low and high damping constant values would allow to obtain states of high and low spin current intensity, respectively. We have fabricated $Fe_{100-x}Co_x$/Ta (with nominal x= 0, 15, 20, 25, 30 and 35) bilayers in which the $Fe_{100-x}Co_x$ layers grow epitaxially and the Ta layer is polycrystalline. We have found the coexistence of Gilbert damping and two magnon scattering mechanisms linked to a sign change in the magnetocrystalline anisotropy constant that allows the manipulation of low and high intensity states of the measured inverse spin Hall effect voltage. Bilayers with lower Co concentrations ($x \leq 25$ %) present different relaxation mechanisms (isotropic Gilbert damping and two magnon scattering) and an extra ferromagnetic resonance linewidth broadening produced due to mosaicity. Bilayers with Co concentration $x > 25$ % present a dominating Gilbert damping for all directions in the film plane. However, in this concentration range the damping constant is anisotropic and when the magnetic field is applied along the hard magnetization direction α increases $\sim$ 420 % with respect to the value obtained for the easy magnetization direction. Coexistence of isotropic Gilbert damping and two magnon scattering generated spin currents 2.5 times larger when the field is applied along the hard magnetization axis compared to the value observed in the easy magnetization axis.

These findings make the $Fe_{100-x}Co_x$/Ta system an excellent candidate for spintronic device applications.

Keywords: anisotropic damping, ferromagnetic resonance, spin current, spin pumping

1. Introduction

The vertiginous development of new electronic devices requires fast data processing, large data storage capacity, miniaturization and low energy consumption [1, 2]. Today, spintronics is one of the principal candidates to solve these problems [3, 4, 5, 6, 7]. In the last decades, an exhaustive search for materials and the study of phenomena that allow the electronic spin manipulation have grown exponentially. An enourmous amount of publications on spin transfer torque (STT), spin orbit torque (SOT), spin pumping (SP), spin Hall effect (SHE) and inverse spin Hall effect (ISHE) studied different aspects of the generation, manipulation and detection of spin currents [4, 5, 6, 7, 8, 9, 10].
SP phenomenon consists in the injection of a pure spin current through the ferromagnetic (FM)/nonmagnetic metal (NM) interface when the ferromagnetic layer fulfills the ferromagnetic resonance (FMR) condition [11, 12, 13, 14, 15, 16]. For applications in spintronics it is desirable that the injected spin current be as high as possible while keeping low input power. The spin current intensity has a strong dependency on the damping parameter ($J_s \propto 1/\alpha^2$), the effective spin mixing conductance ($g^{\uparrow\downarrow}$), the spin Hall angle (Θ_{SH}) and the spin diffusion length (λ_{sd}) [11, 12, 17, 18, 19, 20, 21]. The dependence between J_s and α has motivated the search for materials with low damping constants. Schoen *et al.* [22] reported in 2016 an ultra-low intrinsic magnetic damping constant ($\alpha \sim 5\times10^{-4}$) in polycrystalline FeCo alloys around the $Fe_{75}Co_{25}$ concentration, and related this exceptionally low damping constant value to a sharp minimum of the density of states at the Fermi level. More recently, in 2019 Li *et al.* [23] reported a giant anisotropic Gilbert damping constant in $Fe_{50}Co_{50}$ due to the variation of the spin orbit coupling for different magnetization orientations in the cubic lattice.
In this paper, we present a detailed structural and magnetic characterization of $Fe_{100-x}Co_x$/Ta bilayers for Fe-rich thin films that has been complemented by ISHE-SP measurements. These studies allowed us to determine the presence of different magnetization relaxation mechanisms which have been correlated with the generation of spin currents by spin pumping. We have found that epitaxial $Fe_{100-x}Co_x$ films present anistropic damping for $x >$25 % which can be used to obtain states of high and low spin current intensity when the external field is applied along hard and easy magnetization directions.

2. Experimental details

We deposited by magnetron sputtering a set of five bilayers on MgO [001] single crystal substrates of the form MgO [001]//$Fe_{100-x}Co_x$/Ta. The FeCo layers were deposited

from $Fe_{100-x}Co_x$ alloyed targets with a substrate to target distance of 7.5 cm. The nominal layer thickness was fixed to 20 nm for FeCo and 10 nm for Ta. Films with Co concentration x=15 %, 20 %, 25 %, 30 % and 35 % were deposited and identified according to the percentage of Co as Co15, Co20, Co25, Co30 and Co35. We also fabricated an Fe 99.9 % control sample (called Co0) for additional analysis and conclusions. The base pressure before depositing the samples was $\lesssim 10^{-6}$ Torr. $Fe_{100-x}Co_x$ layers were deposited at a fixed power density of 1.32 W/cm^2 and an Ar pressure of 1.8 mTorr. To improve the epitaxial growth, the FeCo layer was deposited after heating the substrate to a fixed temperature of 423 K. The Ta layer was deposited at room temperature, at 2.6 mTorr of Ar pressure and at 1.76 W/cm^2 of power density. The structural and compositional characterization was performed using a Panalytical Empyrean diffractometer with an eulerian craddle, both with a Cu X-ray tube ($\lambda_{K\alpha}$ Cu = 0.15418 nm) for X-ray diffraction (XRD) and X-ray reflectivity (XRR) measurements, Scanning Transmission Electron Microscopy with High Angular Annular Dark Field (STEM-HAADF), Electron energy-loss spectroscopy (EELS) using a XFEG TITAN 60-300 kV, operated at 300 kV, equipped with monochromator and with a CEOS hexapole aberration corrector for the electron probe. For both STEM-HAADF and EELS analysis, lamellae were prepared using a FIB-SEM microscope model Helios 650 from Thermo Fisher Scientific Company, equipped with a Ga^+ source. The determination of the saturation magnetization (M_s), was carry out using a Lakeshore 7300 vibrating sample magnetometer (VSM). FMR measurements, using a Keysight N9918A vector network analyzer (VNA) or commercial Bruker spectrometers ESP300 (X-, K-, and Q-bands; 9.65 GHz, 24.2 GHz, and 34.8 GHz, respectively) and Elexsys E500 (X-band ∼9.279 GHz), were performed to study the dynamic response. For the measurements with the VNA, a single strip grounded coplanar waveguide was used and the parameter S21 (transmission) was collected in the (2-20) GHz frequency range. In the case of measurements made with spectrometers, the samples were placed in the center of a resonant cavity where the derivative of the absorbed power was measured using a standard field modulation and lock-in detection technique. For the spin pumping-ISHE measurements the samples were cut into small pieces of 1 × 3 mm^2 and a pair of contacts were attached with silver paste at the ends of the sample. More details of the Spin pumping-ISHE characterization can be found in Ref. [24].

3. Results

3.1. Structural characterization

Sample thicknesses were determined by XRR and TEM techniques (see supplemental material). In Table 1 we summarize nominal and measured thicknesses which are in good general agreement. Fig.1a) shows the X-ray $\theta - 2\theta$ pattern for the Co15 sample. Diffraction peaks of the FeCo $(200)_{\mathrm{bcc}}$ film and the MgO $(200)_{\mathrm{fcc}}$ substrate could be identified. The appearance of only the FeCo $(200)_{\mathrm{bcc}}$ reflection in the XRD pattern

Table 1. Nominal and measured composition and thicknesses determined by EELS, XRR and TEM for all the samples under study, respectively.

Sample name	Real composition $Fe_{100-x}Co_x$	Thickness (nm)		
		Nominal FeCo/Ta	XRR FeCo/Ta	TEM FeCo/Ta
Co15 ($Fe_{85}Co_{15}$)	$x = 17(1)$	20/10	18(1)/9(1)	19(1)/9(1)
Co20 ($Fe_{80}Co_{20}$)	$x = 20(1)$	20/10	20(1)/11(1)	21(1)/12(1)
Co25 ($Fe_{75}Co_{25}$)	$x = 26(1)$	20/10	19(1)/8(1)	21(1)/9(1)
Co30 ($Fe_{70}Co_{30}$)	$x = 29(1)$	20/10	18(1)/9(1)	19(1)/9(1)
Co35 ($Fe_{65}Co_{35}$)	$x = 34(1)$	20/10	19(1)/10(1)	20(1)/10(1)

strongly suggests an epitaxial growth on the MgO (100) substrate. From the FeCo $(200)_{\rm bcc}$ peaks we estimated the lattice parameter a of all samples. The average value obtained was $a = 0.286(1)$ nm, with no systematic variation as a function of x. The value obtained is in well agreement with those reported for this range of concentrations ($a \sim 0.286$ - 0.287 nm) [22]. In a previous work [25] we found that the $Fe_{80}Co_{20}$ film presented epitaxial growth on MgO with the [100] FeCo axis rotated by 45° with respect to the MgO [100] substrate direction. This rotation was verified in all films by performing X-ray ϕ-scan experiments. We can see in Fig.1b) that the $(110)_{\rm bcc}$ $Fe_{85}Co_{15}$ peaks (dashed line) are intercalated every 45° with the $(220)_{\rm fcc}$ MgO (solid lines) peaks. In Fig.1c) we show a cross section TEM image of the Co15 sample, where we can observe that approximately 2 nm of the Ta layer exposed to air tend to oxidize forming a TaO_x capping layer on top of each bilayer (Fig.1d)). Fig.1c)-e) shows the good quality of FeCo/Ta and FeCo/MgO interfaces, with a roughness in the range of 1 nm. FeCo shows to be epitaxial, while Ta shows a mixture of β-Ta and α-Ta in nanocrystal size. Using HRTEM techniques (Fig.1e)), it was found that all FeCo films present a chemically disordered bcc structure in their A2 cubic phase with small regions with ordered DO_3 phase. The ordered DO_3 phase corresponds to the thermodynamic equilibrium phase and is expected to occur for the stoichiometric alloy $Fe_{75}Co_{25}$ [26] (see supplemental material for more information about structural properties of FeCo and Ta layers). In our case, films were deposited at 423 K, so the temperature was not large enough to promote the full order of this phase. Anyway, small regions with DO_3 phase were observed in some of the films. The relative concentrations of Fe and Co were determined by EELS, obtaining a good agreement between nominal and measured values in the deposited films (Fig.1f)). The real composition of each sample was summarized in Table 1.

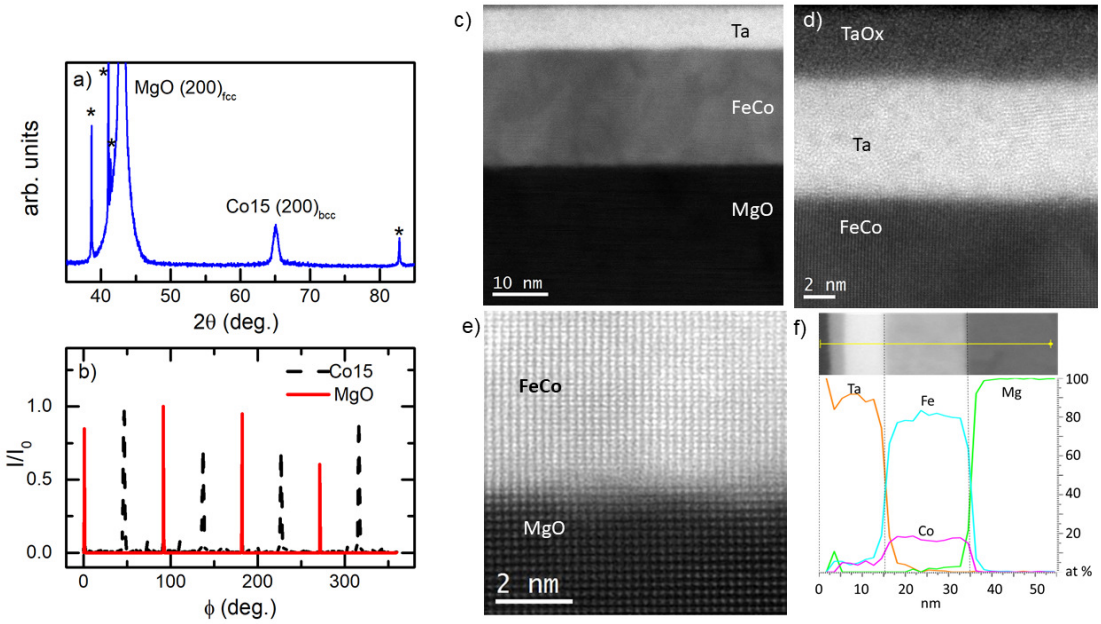

Figure 1. a) XRD pattern for the sample Co15. The peaks marked with (∗) are (200) and (400) reflections of the MgO substrate due to partially unfiltered radiation from lines Cu-K_β and W-L_α of the Cu anode. b) Normalized intensity vs. ϕ angle (ϕ-scan experiment) for $Fe_{85}Co_{15}$ $(110)_{\rm bcc}$ (dashed line) and MgO $(220)_{\rm fcc}$ (solid line) diffraction peaks. For this experiment the sample was rotated by 45° in the angle χ to put the {110} family of planes in diffraction condition. c) Cross section TEM image of Co15 sample. d)-e) High resolution cross section TEM image. We can observe that approximately 2 nm of the Ta layer exposed to air tend to oxidize forming a TaO_x capping layer on top of each bilayer. Note the good quality of the samples evidenced by the small roughness ($\lesssim$ 1 nm) of the interfaces and the good epitaxiality of FeCo on the MgO substrate. f) Cross section concentration profile determined by EELS for the sample Co15.

3.2. FMR measurements and analysis

The classical Landau-Lifshitz-Gilbert equation of motion is generally used to describe the dynamics of the magnetization vector [27]:

$$\frac{d\mathbf{M}}{dt} = -\gamma\mathbf{M}\times\left(\mathbf{H}_{\rm t} - \frac{\alpha}{\gamma M}\frac{d\mathbf{M}}{dt}\right), \tag{1}$$

where α is the damping parameter, $\gamma = \frac{g\mu_\beta}{\hbar}$ is the gyromagnetic factor, $\mathbf{M}$ the magnetization vector, and $\mathbf{H}_{\rm t}$ is the total magnetic field (that includes the external field and contributions arising from anisotropies). Using the Smit and Beljers formalism [28], equation 1 can be solved for the uniform mode of precession. To obtain the dispersion relation we propose a magnetic free energy of the form:

$$F(\theta,\varphi) = -MH\sin\theta\cos(\varphi-\varphi_H)+2\pi M^2\cos^2\theta-K_u\sin^2\theta\cos^2\varphi-K_c\left(\frac{\sin^2 2\theta+\sin^2 2\varphi\sin^4\theta}{4}\right), \tag{2}$$

where we consider the Zeeman energy of the magnetization $\mathbf{M}$ in an external field $\mathbf{H}$, characterized by an in-plane angle φ_H, (first term in equation 2), the shape energy

given by the demagnetization factor of a thin film (second term in equation 2) and the uniaxial and cubic energies characterized by the anisotropy constants of uniaxial and cubic symmetry K_u and K_c, respectively (third and fourth terms in equation 2). φ is the azimuthal angle that forms the projection of $\mathbf{M}$ with the spherical coordinate system ($\varphi = 0$ corresponding to the MgO [100] direction), and θ is the out of plane polar angle. For K_u and $K_c > 0$ these anisotropy terms describe an easy axis parallel to MgO [100] and a cubic anisotropy with easy axes parallel to the MgO [110] directions, respectively. Substituting equation 2 in the Smit and Beljers equation [28] we can obtain the dispersion relation for our system when the field H is applied in the film plane:

$$\left(\frac{\omega}{\gamma}\right)^2 = \left[H\cos(\varphi-\varphi_H) + H_u\cos^2\varphi - H_c\left(1-\frac{\sin^2 2\varphi}{2}\right)\right]\times\left[H\cos(\varphi-\varphi_H) + H_u\cos 2\varphi - H_c\cos 4\varphi\right], \quad (3)$$

where H_u and H_c are the uniaxial and cubic anisotropy fields defined as $H_u = \frac{2K_u}{M}$ and $H_c = \frac{2K_c}{M}$, respectively, and $\omega = 2\pi f$ where f is the excitation frequency. A schematics of the magnetic field and magnetization vectors with respect to the MgO crystalline axes is shown in Fig. 2.

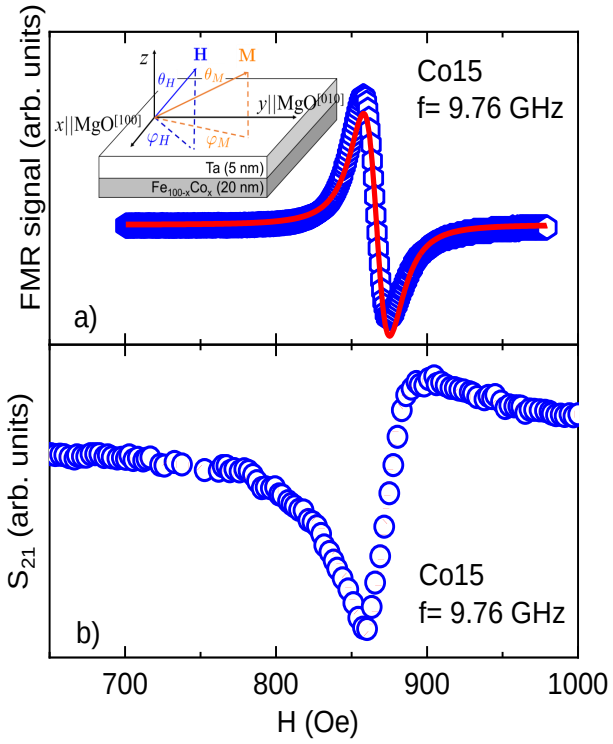

Figure 2. Spectra collected for the Co15 sample. a) Using a spectrometer with field modulation and a resonator at 9.76 GHz (X-band). The solid line represents the fit using a derivative Lorentzian lineshape. Inset: Schematics of the magnetic field and magnetization vectors and the coordinate axes with respect to the MgO crystalline axes. b) Same sample using a VNA at 9.76 GHz. The dotted line corresponds to the fit of the absorption curve described by the addition of a symmetrical and an anti-symmetrical Lorentzian curve [29].

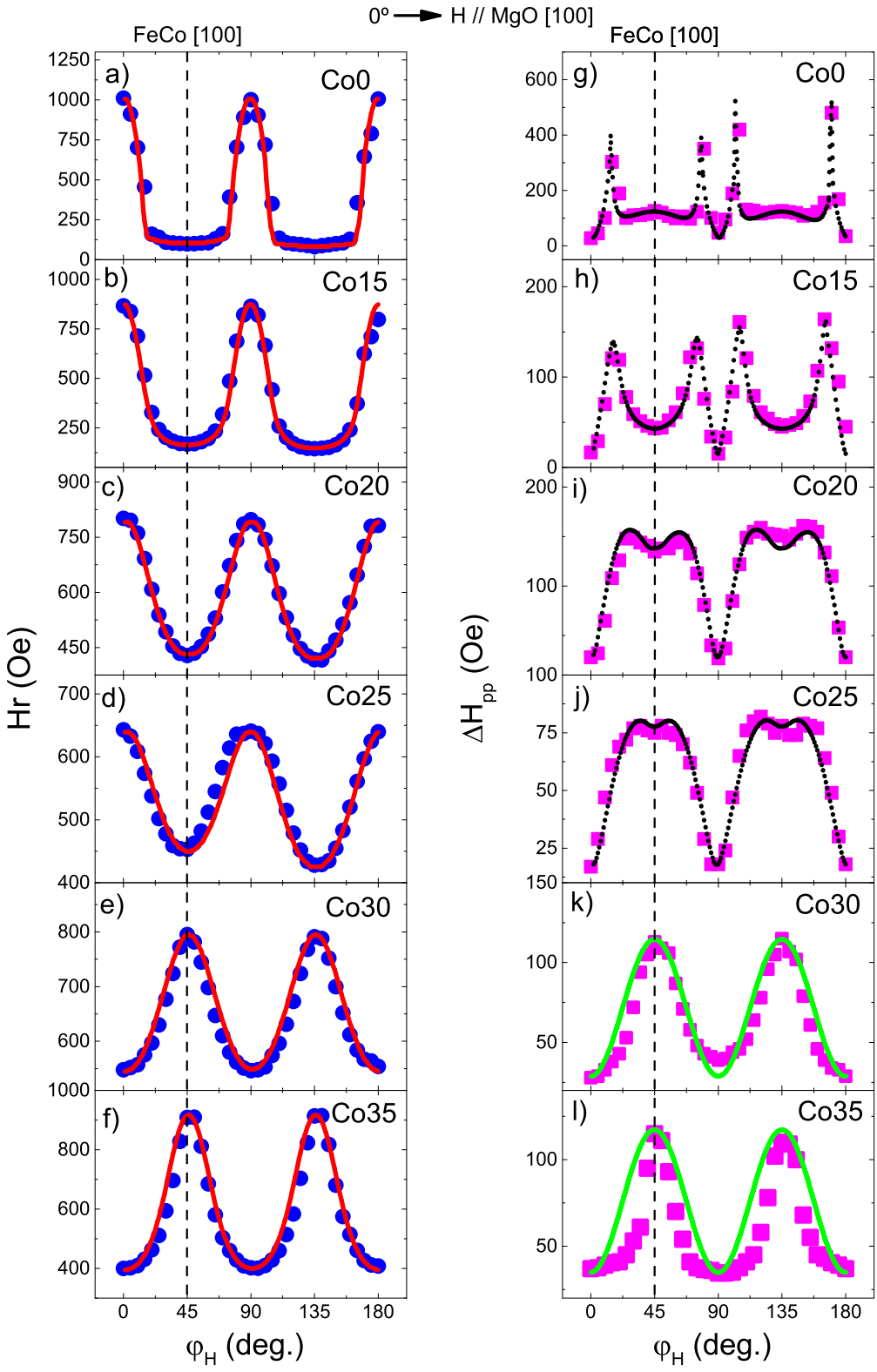

Figure 3. a)-f) In-plane angular variation of the FMR resonance field for the samples under study. The solid lines represent the fit using equation 3. g)-i) In-plane angular variation of the FMR peak to peak linewidth for the samples under study. Dotted lines in panels g)-j) represent the fit using the phenomenological model described in Ref. [25]. Solid lines in plots k) and l) have been obtained from Eq. 7.

FMR spectra were collected with both an X-band (9.76 GHz) spectrometer with field modulation (Fig.2a)) and a coplanar wave guide using a VNA in transmission mode in the 2 GHz - 20 GHz frequency range (Fig.2b)). Data were fitted by assuming a complex susceptibility second derivative line shape (solid line in Fig.2a)) and using an absorption peak curve described by the addition of symmetrical and anti-symmetrical Lorentzian curves [29] (dotted line in Fig.2b)). In order to gain insight into the magnetic anisotropies of our system as well as the mechanisms that may contribute to damping, we have performed FMR angular dependence on the X-band spectrometer. Fig.3a)-3f) show the results of the in-plane angular variation of the FMR resonance field for the samples under study. We can see that all samples present fourfold symmetry with the presence of a weak uniaxial anisotropy. In Fig.3 the angle $\varphi_H = 0°$ indicates that the external magnetic field is parallel to the MgO [100] direction (**H** $\parallel$ MgO [100]). As we previously mentioned, all the samples grow with the FeCo [100] direction rotated by 45° with respect to the MgO [100] axis (see Fig. 1(b)). The fact that Co-richer samples (Co30 and Co35) also present an easy axis rotated by 45° (Fig.3e)-3f)) compared to Fe-richer (Co0 - Co25) samples (Fig.3a)-3d) indicates a sign change in the cubic magnetocrystalline anisotropy constant K_c. Using equation 3 we can fit the angular variation of the FMR resonance field data (solid lines in Fig.3a)-3f)) to obtain the $H_c = 2K_c/M$ concentration dependence that is shown in Fig.4. For the fit with Eq.3, we used the saturation magnetization (M_s) values obtained by vibrating sample magnetometry (VSM) (see supplemental material), with an average value $M_s \sim$ 1700 emu/cm^3. For $Fe_{100-x}Co_x$ bulk alloys the sign change in K_c takes place at a Co concentration [30] $x \sim 45\%$ (solid stars in Fig.4). For thin films the change was reported previously by Pelzl *et al.* [31] around $x \sim 33\%$ and the difference between bulk and thin films zero crossing is attributed to the thickness dependence of the magnetocrystalline anisotropy field, which decreases as the thickness decreases [31].

In our case, the zero crossing takes place between 25% and 30% of Co concentration. It is well known that low dimensionality can lead to discrepancies between the values obtained for bulk materials and thin films. Nevertheless, in a previous work [21] made on $Fe_{80}Co_{20}$ thin films for different thicknesses (4 nm - 12 nm) no thickness dependence was observed, but probably the explored thickness range was not large enough to obtain conclusions about the dependence of K_c with film thickness.

The results of the in-plane angular variations of the FMR peak to peak linewidth (ΔH_{pp}) for the samples under study are shown in Fig.3g)-3i). A gradual change in the angular behavior of ΔH_{pp} is observed. Note, however, that the samples Co0, Co15, Co20 and Co25 present a minimum in ΔH_{pp} value when **H** is applied parallel to the FeCo [110] hard axis. In turn, ΔH_{pp} increases as we approach the [100] easy axis, having the maximum value at an intermediate angle. This behavior was previously observed in $Fe_{80}Co_{20}$/Ta bilayers [25] and was explained in terms of the influence of the intrinsic Gilbert damping relaxation mechanism in addition to extrinsic two magnon scattering relaxation and mosaicity linewidth broadening. [32, 33, 34, 35, 36]. The dotted lines in Fig.3g)-3j) show the fits using this phenomenological model. In the case of Co-rich

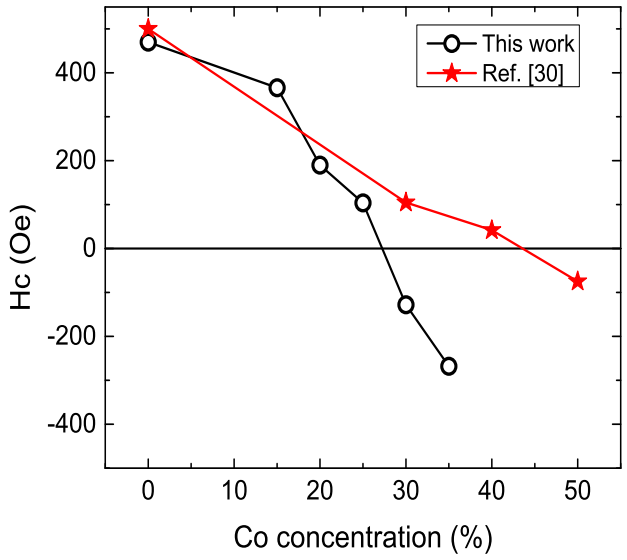

Figure 4. Cubic anisotropy field as a function of Co concentration. Data for thin films (open circles-this work) and bulk samples [30] (solid stars).

samples (Co30 and Co35) (Fig.3k)-3l)), ΔH_{pp} presents a minimum and maximum along the easy and hard magnetization directions, respectively. In Ref. [23] this behavior in ΔH_{pp} was attributed to a giant anisotropy of the Gilbert damping constant in epitaxial $Fe_{50}Co_{50}$ thin films and was ascribed to the variation of the spin orbit coupling for different cubic lattice magnetization orientations. The general dependence of ΔH_{pp} with ω is given by:

$$\Delta H_{pp} = \Delta H_0 + \Delta H_{2M}(\omega, \varphi_H) + \frac{2}{\sqrt{3}} \frac{1}{\partial \frac{\omega}{\gamma}/\partial H} \Delta \frac{\omega}{\gamma}, \tag{4}$$

where the first term describes all frequency independent extrinsic contributions related to distributions of anisotropy constants and anisotropy axes, saturation magnetization, etc. [37]. The second term is a non linear frequency dependent extrinsic contribution that arises from two magnon scattering mechanisms [25, 33, 34]. The third term describes the intrinsic damping (Gilbert damping) that is linear with frequency. In the case of weak uniaxial and cubic anisotropies it is given by [19, 38]:

$$\frac{1}{\partial \frac{\omega}{\gamma}/\partial H} \Delta \frac{\omega}{\gamma} = \frac{1}{\partial \frac{\omega}{\gamma}/\partial H} \frac{\alpha_{\rm tot}}{2M} \left(\frac{\partial^2 F}{\partial \theta^2} - \frac{1}{\sin^2 \theta} \frac{\partial^2 F}{\partial \varphi^2} \right) = \alpha_{\rm tot} \frac{\omega}{\gamma} \frac{1}{\cos(\varphi - \varphi_H)} \sim \alpha_{\rm tot} \frac{\omega}{\gamma}. \tag{5}$$

Then, Eq. 4 can be approximated by:

$$\Delta H_{pp} = \Delta H_0 + \Delta H_{2M}(\omega, \varphi_H) + \frac{2}{\sqrt{3}} \alpha_{\rm tot} \frac{\omega}{\gamma}. \tag{6}$$

The last term in Eq. 6 assumes an isotropic Gilbert damping constant which should be corrected to describe the ΔH_{pp} angular dependence of the samples Co30 and Co35.

Following Ref. [23], we propose an expression that takes into account a giant anisotropic Gilbert damping constant and the cubic symmetry of the crystal:

$$\Delta H_{pp} = \Delta H_0 + \frac{2}{\sqrt{3}}\frac{\omega}{\gamma}\left[\alpha_{\text{easy}} + (\alpha_{\text{hard}} - \alpha_{\text{easy}})\sin^2(2\varphi)\right], \tag{7}$$

where α_{easy} and α_{hard} are the Gilbert damping parameters when the external magnetic field is applied along the easy and hard magnetization directions, respectively. The dotted lines in Fig. 3k)-l) represent the fit using Eq.7, from which we obtain α_{easy} and α_{hard} values. For intermediate angles the proposed model is not very accurate (particularly for Co35) which could be due to unsaturated magnetization effects for intermediate angles at relatively low frequencies (9.76 GHz). In order to test this assumption, we performed ΔH_{pp} angular variations at a higher frequency (34.9 GHz) and we have found that the experimental data are very well described by Eq.7 (see supplemental material).

In order to investigate the Co concentration variation of the damping parameter, we show in Fig. 5 the ΔH_r vs. $\frac{\omega}{\gamma}$ dependence for the samples Co15, Co25 and Co35. For clarity, in Fig.5 we distinguished between $\mathbf{H} \parallel$ FeCo hard axis (full symbols), $\mathbf{H} \parallel$ easy axis (open symbols), respectively. The solid lines represent the fits using Eq.6 with the $\Delta H_r = \frac{\sqrt{3}}{2}\Delta H_{pp}$ correction for Lorentzian curves. For the samples Co15 and Co25 it can be observed that when the external field is applied along the hard axis (full symbols in Fig.5a)-5b)), the linear model described by Eq.6 is fulfilled. For the easy directions (open symbols in Fig.5a)-5b)) a non-linear dependence is found. As we already mentioned, this behavior can be explained in terms of the two magnon scattering mechanism. The dashed lines in Fig.5a)-5b) have been obtained using Eq.6 with a single α value and the addition of the two magnon scattering mechanism given by [25]:

$$\Delta H_{2M}(\omega, \varphi_H) = \Gamma \sin^2 2\varphi_H \sin^{-1}\left[\sqrt{\frac{\sqrt{\omega^2 + \left(\frac{\omega_0}{2}\right)^2} - \frac{\omega_0}{2}}{\sqrt{\omega^2 + \left(\frac{\omega_0}{2}\right)^2} + \frac{\omega_0}{2}}}\right], \tag{8}$$

where $\omega_0 = \gamma 4\pi M_{\text{eff}}$ with M_{eff} the effective magnetization. The factor Γ is the strength of the two magnon scattering, and the term $\sin^2 2\varphi_H$ gives the behavior of ΔH_{2M} according to the direction of H with respect to the principal in-plane crystallographic directions.

The FMR linewidth (ΔH_r) frequency dependence for the sample Co35 shows a linear dependence in both, easy and hard directions and the minimum linewidth is in the easy direction. These observations suggest that two magnon scattering is not an important relaxation mechanism in these films. Samples Co30 and Co35 have a similar behavior, that shows an increase in the damping constant of 320 % and 420 % between easy and hard magnetization directions, respectively. These values of the Gilbert damping constant anisotropy are of the same order than those reported in Ref. [23]. This behavior supports the idea that above a critical Co concentration $x \sim 30$ % in our samples, a giant anisotropic Gilbert damping constant emerges as the main relaxation mechanism. Fig.6 shows the calculated α values (hexagons) as

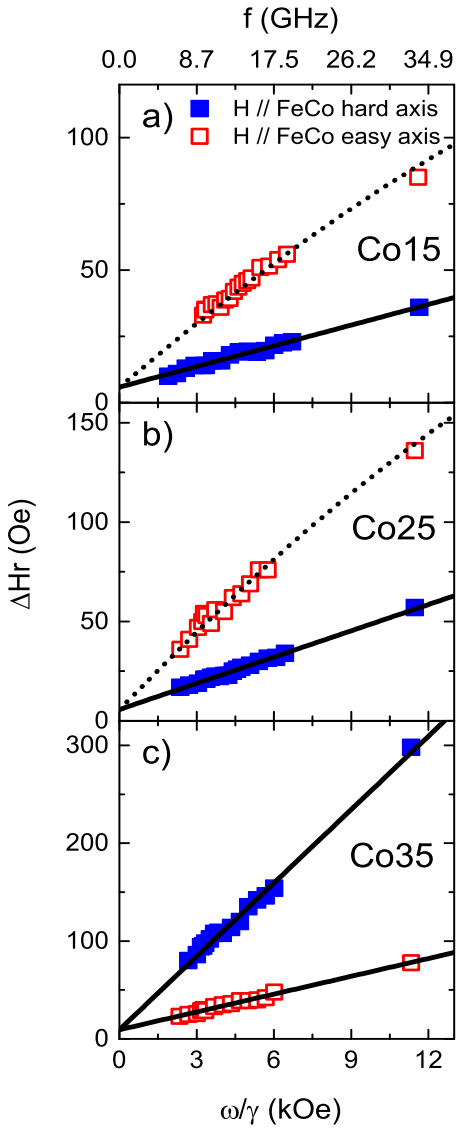

Figure 5. Frequency dependence of the FMR linewidth for the samples Co15, Co25 and Co35. Solid lines represent the fit using the linear model described by Eq.6. Dotted curves represent the fit using the linear model with the addition of the two magnon scattering mechanism.

a function of the Co concentration for the samples under study. The parameter α is usually called the total Gilbert damping constant ($\alpha_{\rm tot}$) since it includes other contributions to the intrinsic Gilbert damping constant ($\alpha_{\rm int}$) such as the spin pumping contribution $\alpha_{\rm sp}$ and the radiative contribution $\alpha_{\rm rad}$, so that α can be written as $\alpha = \alpha_{\rm tot} = \alpha_{\rm int} + \alpha_{\rm sp} + \alpha_{\rm rad}$. $\alpha_{\rm rad}$ is an extra contribution due to the inductive coupling of the precessing magnetization and the coplanar waveguide [22, 39]. In our case we have done measurements using both a coplanar waveguide and a resonant cavity (where this contribution is zero), the match between data extracted with both methods

lead us to discard this term. $\alpha_{\rm sp}$ is an extra relaxation mechanism due to the spin pumping phenomenon that can be subtracted knowing the spin mixing conductance ($g^{\uparrow\downarrow}$) of the $Fe_{100-x}Co_x$/Ta interface and the $Fe_{100-x}Co_x$ thickness [40, 41, 42]. To extract the $\alpha_{\rm sp}$ contribution we used $g^{\uparrow\downarrow} = 5.7(3) \times 10^{14}$ cm^{-2} determined in a previous work in $Fe_{80}Co_{20}$/Ta bilayers[25]. Here we assumed that $g^{\uparrow\downarrow}$ is the same for different Co concentrations, according to the results published in Fig. S4 of Ref.[22]. Fig. 6 shows the Gilbert damping parameter as a function of Co concentration. We present $\alpha_{\rm tot}$ (hexagons) and $\alpha_{\rm int} = \alpha_{\rm tot} - \alpha_{\rm sp}$ (stars) for the samples under study. The figure shows the minimum $\alpha_{\rm int}$ value estimated for each sample where solid and open symbols indicate that the minimum value was obtained for a hard or an easy magnetization direction, respectively. An exceptionally low intrinsic damping $\alpha_{\rm int} = 5(2) \times 10^{-4}$ was obtained for the Co15 film. Schoen *et al.* [22] found a minimum $\alpha_{\rm int}$ value at a 25 % Co concentration (solid squares in Fig. 6) associated to a sharp minimum in the density of states at the Fermi level. On the other hand, Mankovsky *et al.* [43] using the fully relativistic KKR (Korringa-Kohn-Rostoker formalism) band structure method in combination with the CPA (coherent potential approximation) alloy theory predicted a minimum between 10 % - 15 % Co concentration at 0 K (solid circles in Fig. 6). Our experimental results show a minimum in $\alpha_{\rm int}$ for a 15 % Co concentration and in the 0 % - 20 % range the estimated values are in good agreement with those reports, but for $x \geq 25$ % our data disagrees with previous results. Mankovsky *et al.* [43] argue that the coexistence of two phases (see section 3.1) can modify the minimum of the density of states at the Fermi level and, consequently, the $\alpha_{\rm int}$ Co concentration dependence. It is possible that the coexistence of A2 and DO_3 phases, the monocrystalline nature of our samples and the sign change in K_c contribute to the discrepancy observed at high Co concentrations.

In Table 2 we summarize relevant parameters obtained in this work for the samples under study. Two magnon scattering strength Γ increases systematically as the Co concentration increases. The Γ parameter is not expected to depend on the Co concentration because it is a extrinsic relaxation mechanism related to the concentration of magnetic impurities [33, 34, 25]. But we can not rule out that the samples Co0, Co15, Co20 and Co25 present some degree of anisotropic damping that increases with the Co concentration. Because the two magnon scattering contribution is dominant for these samples it was not possible to separate these two contributions and, consequently, the Γ parameter could be overestimated as the Co concentration increases.

3.3. ISHE voltage measurements

As we discussed in the previous section, different relaxation mechanisms act when the external field is applied along the easy or hard magnetization directions. To know if the conversion efficiency is also anisotropic, we then performed measurements with H applied parallel to MgO [100] or [110] and $V_{\rm ISHE}$ measured in the [010] and [1$\bar{1}$0] directions, respectively (see inset in Fig.7). Measurements were made in a resonator

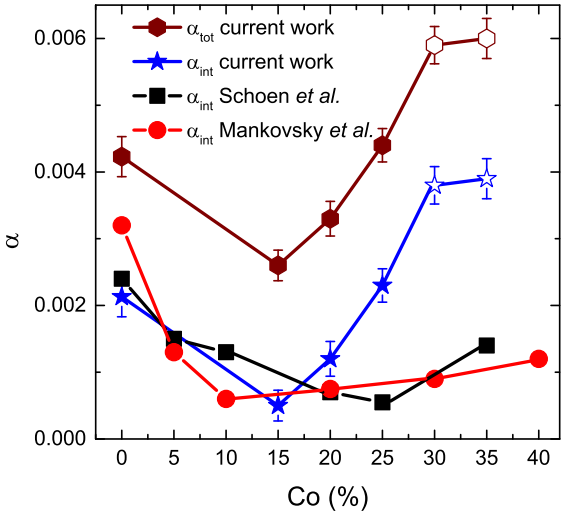

Figure 6. Gilbert damping parameter as a function of the Co concentration. We present the minimum α value obtained for each sample. Solid and open symbols are for data obtained in a hard or an easy magnetization direction, respectively. Hexagons and stars represent the total and intrinsic Gilbert damping parameters $\alpha_{\rm tot}$ and $\alpha_{\rm int}$, respectively. We also show experimental (solid squares) and theoretical (solid circles) $\alpha_{\rm int}$ values obtained from Refs. [22] and [43].

Table 2. Values of g, $H_{\rm c}$, $\alpha_{\rm easy}$, $\alpha_{\rm hard}$, Γ and $I^{\rm max}_{\rm ISHE}/I^{\rm min}_{\rm ISHE}$ obtained in this work.

Sample	g	$H_{\rm c}$ (Oe)	$\alpha_{\rm easy}$	$\alpha_{\rm hard}$	Γ (Oe)	$\delta I_{\rm ISHE}$
Co0	2.085(4)	470(40)	0.0042(4)	0.0042(4)	95(10)	2.49(5)
Co15	2.088(3)	366(20)	0.0026(3)	0.0026(3)	118(15)	2.67(3)
Co20	2.094(5)	200(10)	0.0033(4)	0.0033(4)	160(20)	1.81(4)
Co25	2.110(3)	110(8)	0.0044(4)	0.0044(4)	180(20)	1.84(4)
Co30	2.125(2)	-80(5)	0.0059(6)	0.0191(7)	-	1.55(4)
Co35	2.139(4)	-280(20)	0.0061(6)	0.0252(8)	-	1.04(4)

with the microwave power fixed at 100 mW. Using these two configurations we obtained the curves $V_{\rm ISHE}$ vs. H shown in Fig.7a)-7d). The maximum value of $V_{\rm ISHE}$ was obtained in the direction where damping is minimum. This behavior is due to the spin current density intensity J_s dependence with damping[21, 20]:

$$J_s = \gamma \frac{\hbar}{4\pi} g^{\uparrow\downarrow} \left(\frac{h_{\rm rf}}{\alpha}\right)^2 \frac{M F_{\varphi\varphi}}{\left[F_{\theta\theta} + F_{\varphi\varphi}\right]^2}, \tag{9}$$

where $F_{\varphi\varphi}$ and $F_{\theta\theta}$ are the second partial derivatives of the free energy with respect to the spherical angles (θ and φ) evaluated at the equilibrium angles ($\theta_{\rm eq}$ and $\varphi_{\rm eq}$) of the magnetization vector.

In Eq.9 we used the free energy expression (Eq.2) for the in-plane configuration (the external magnetic field always lies in the plane of the sample (see inset in Fig.7)).

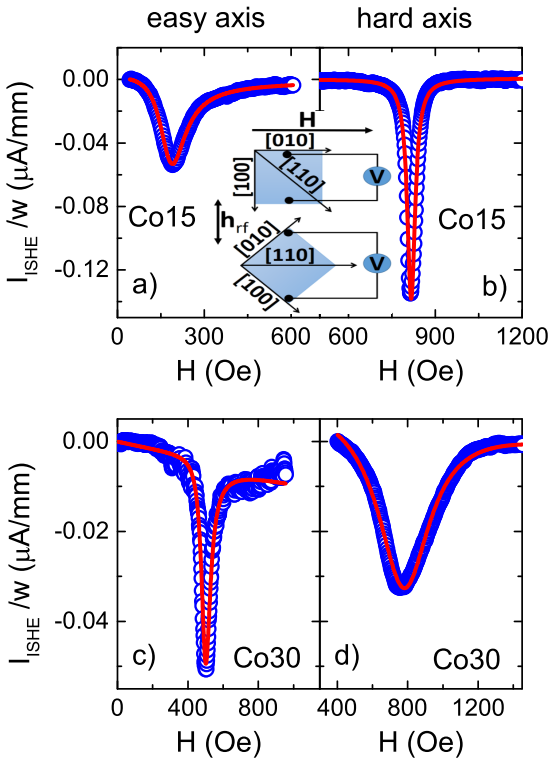

Figure 7. a)-d) I_{ISHE} measurements for the samples Co15 and Co30 for the two configurations shown in the inset. Data were normalized for the sample width (w) for comparative purposes. The inset shows the two configurations used for V_{ISHE} measurements. We fixed two electrodes on top of the Ta layer for detection of the V_{ISHE} signal perpendicular to the applied external field (**H** ∥ MgO [010] and [110] directions).

Note that in Eq.9 we have assumed that $g^{\uparrow\downarrow}$ is constant for different IP orientations of the magnetic field.

In order to corroborate the $J_s \propto \frac{1}{\alpha^2}$ dependence in Eq.9 we plotted (see Fig.8a)) the inverse spin Hall effect current $I_{\mathrm{ISHE}}/w = V_{\mathrm{ISHE}}/(wR)$ (R is the total electrical resistance measured between electrodes and w is the sample width) as a function of $\frac{1}{\alpha^2}$ for the samples under study. According to the inset of Fig.7 and the stacking order of our samples, the negative sign of I_{ISHE} is due to the negative value of Θ_{SH} (Ta). Directions that could be described by a linear Gilbert damping model are represented with open circles and show the expected $\frac{1}{\alpha^2}$ linear dependence. From the linear fit we extracted the slope value -6.53(4) $\times$ $10^{-7}\mu$A, which is in good agreement with the calculated value (-5.13 $\times$ $10^{-7}\mu$A) using Eq.17 from Ref. [21] and parameters obtained in a previous work on $Fe_{80}Co_{20}$/Ta bilayers [21]. Solid circles indicate the directions where Gilbert damping plus two magnon scattering mechanisms were needed to describe the experimental behavior. In this case I_{ISHE} is almost constant with the damping. In

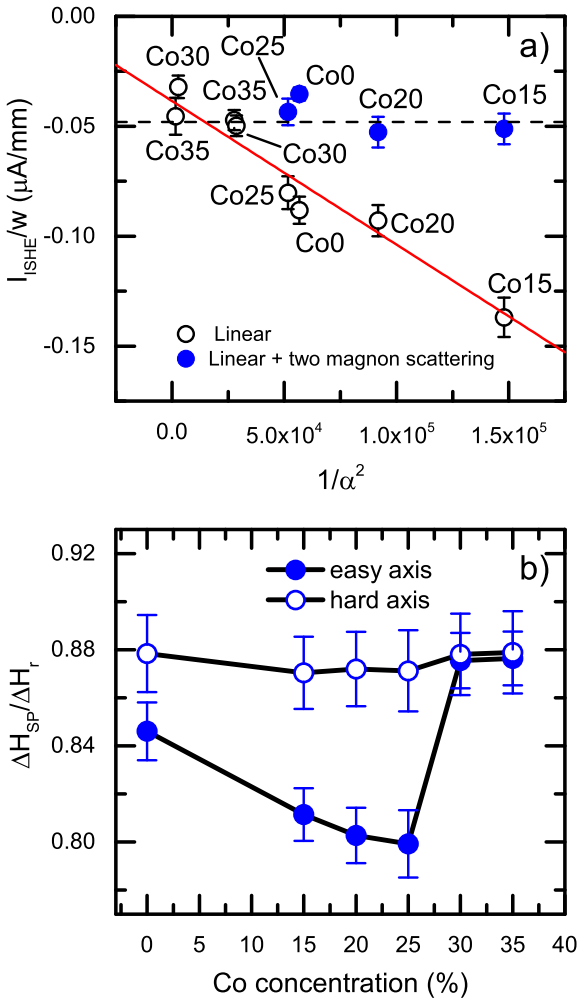

Figure 8. a) I_{ISHE}/w vs. $\frac{1}{\alpha^2}$ for the samples under study. Open circles represent the samples and their corresponding directions where only linear Gilbert damping model was used for the estimation of α. Solid circles represent data for which linear Gilbert damping and two magnon scattering models were used for α estimation. b) $\Delta H_{\mathrm{SP}}/\Delta H_r$ ratio of the linewidths obtained from SP voltage measurements and FMR spectra as a function of Co concentration for the samples under study. Open and solid circles represent hard and easy magnetization directions, respectively.

order to discuss the obtained results, we show in Fig. 8b) the ratio $\Delta H_{\mathrm{SP}}/\Delta H_r$ as a function of the Co concentration, where ΔH_r and ΔH_{SP} are the FWHM FMR and V_{ISHE} signal linewidths, respectively. We can observe that the directions described by a linear Gilbert damping model present a relative constant value $\Delta H_{\mathrm{SP}}/\Delta H_r \sim 0.9$, which is close to the expected value ~ 1 when only the intrinsic damping is present. Directions described by a linear Gilbert damping plus two magnon scattering mechanisms show a smaller $\Delta H_{\mathrm{SP}}/\Delta H_r$ ratio that decreases with Co concentration. The fact that the

$\Delta H_{\mathrm{SP}}/\Delta H_r$ ratio decreases as the two magnon scattering strength Γ increases (see table 2), could be an indication that the extrinsic mechanisms are less efficient to generate a spin current.

Despite the previous analysis, it should be noted that the ratio $\Delta H_{\mathrm{SP}}/\Delta H_r$ is still close to one and the difference between ΔH_{SP} and ΔH_r could be due to the uncertainties in fitting non symmetrical line shapes. In any case, what it is important to mention is that films in which the two magnon scattering process is needed to explain the FMR linewidth do not follow a $\frac{1}{\alpha^2}$ dependence and they could not be described by a distribution that preserves the area of the absorption line. In this context, further analysis is necessary in order to elucidate these results.

The main achievement of the present work has been not only to control the spin current intensity but also to obtain states of low and high I_{ISHE} values. For the sake of comparison, we define the ratio between maximum ($I^{\mathrm{max}}_{\mathrm{ISHE}}$) and minimum ($I^{\mathrm{min}}_{\mathrm{ISHE}}$) values of the generated current, obtained when the external field is applied along the hard and easy magnetization directions. The ratios $\delta I_{\mathrm{ISHE}} = I^{\mathrm{max}}_{\mathrm{ISHE}}/I^{\mathrm{min}}_{\mathrm{ISHE}}$ are summarized in Table 2. The δI_{ISHE} quantity gives us an idea of how big is the difference between high and low intensity spin current states. We can conclude that the coexistence of the linear Gilbert damping and two magnon scattering mechanisms produces a larger value of δI_{ISHE}, obtaining the highest value for the Co15 bilayer. Moreover, these rather interesting results are in sharp contrast to simple magnetic epitaxial layers as in Fe/Pt where isotropic damping and $g^{\uparrow\downarrow}$ have been reported as well as spin-orbit torque depending on the easy or hard directions turned out to be isotropic [44].

4. Conclusions

In summary, through the coexistence of different relaxation mechanisms in $Fe_{100-x}Co_x$/Ta bilayers, it was possible to manipulate the spin current intensity generated by the spin pumping phenomenon. We obtained an exceptionally low $\alpha_{\mathrm{int}} = 5(2) \times 10^{-4}$ value that allowed us to produce a high intensity spin current injection. We observed that the coexistence of intrinsic and extrinsic relaxation mechanisms is more efficient for obtaining states of high and low spin current intensity than the existence of a giant Gilbert damping anisotropy. We obtain $\delta I_{\mathrm{ISHE}} = I^{\mathrm{max}}_{\mathrm{ISHE}}/I^{\mathrm{min}}_{\mathrm{ISHE}} = 2.67(3)$ for the sample Co15, which is a remarkable result in terms of spin current manipulation. The possibility to tune the J_s injected and the overall spin current to charge conversion efficiency is one of the main goals of today's spintronics. Here we are reporting the possibility to tune both in the very same system just playing with the crystallographic orientation, making $Fe_{100-x}Co_x$/Ta system an excellent and robust candidate for spintronic devices applications.

Acknowledgments

Technical support from Rubén E. Benavides, César Pérez, and Matías Guillén is greatly acknowledged. L. M. is with the Laboratorio de Investigación Aplicada en Telecomunicaciones-LIAT (DIT, GDTyPE, GAIyANN, CNEA). This work was partially supported by Conicet under Grant PIBAA 2022-2023 project MAGNETS Grant ID. 28720210100099CO; ANPCyT Grant PICT-2018-01138, ANPCyT Grant PICT 2021-00113 (project DISCO) and U.N. Cuyo Grant 06/C556 from Argentina. We acknowledge the financial support of European Commission by the H2020-MSCA RISE project ULTIMATE-I (Grant No. 101007825). Authors would like to acknowledge the use of Servicio General de Apoyo a la Investigación-SAI, Universidad de Zaragoza.

Bibliography

[1] J. Puebla, J. Kim, K. Kondou, and Y. Otani. Spintronic devices for energy-efficient data storage and energy harvesting. *Commun. Mater.*, 1(1):1–9, 2020.

[2] D. E. Speliotis. Magnetic recording beyond the first 100 years. *J. Magn. Magn. Mater.*, 193(1-3):29–35, 1999.

[3] R. P. Cowburn. Change of direction. *Nat. Mater.*, 6(4):255–256, 2007.

[4] S. Bhatti, R. Sbiaa, A. Hirohata, H. Ohno, S. Fukami, and S. N. Piramanayagam. Spintronics based random access memory: a review. *Mater Today*, 20(9):530–548, 2017.

[5] V. K. Joshi. Spintronics: A contemporary review of emerging electronics devices. *Eng. Sci. Technol. an Int. J.*, 19(3):1503–1513, 2016.

[6] M. Eschrig. Spin-polarized supercurrents for spintronics: a review of current progress. *Rep. Prog. Phys.*, 78(10):104501, 2015.

[7] A. Hirohata, K. Yamada, Y. Nakatani, I. L. Prejbeanu, B. Diény, P. Pirro, and B. Hillebrands. Review on spintronics: Principles and device applications. *J. Magn. Magn. Mater.*, 509:166711, 2020.

[8] S. D. Bader and S. S. P. Parkin. Spintronics. *Annu. Rev. Condens. Matter Phys.*, 1(1):71–88, 2010.

[9] L. B. Chandrasekar, K. Gnanasekar, and M. Karunakaran. Spintronics: A mini review. *Superlattices Microstruct.*, 136:106322, 2019.

[10] C. Felser, G. H. Fecher, and B. Balke. Spintronics: a challenge for materials science and solid-state chemistry. *Angew. Chem. Int. Ed.*, 46(5):668–699, 2007.

[11] Y. Tserkovnyak, A. Brataas, and G. E. W. Bauer. Enhanced Gilbert damping in thin ferromagnetic films. *Phys. Rev. Lett.*, 88(11):117601, 2002.

[12] E. Saitoh, M. Ueda, H. Miyajima, and G. Tatara. Conversion of spin current into charge current at room temperature: Inverse spin-Hall effect. *Appl. Phys. Lett.*, 88(18):182509, 2006.

[13] F. Yang and P. C. Hammel. FMR-driven spin pumping in Y3Fe5O12-based structures. *J. Phys. D: Appl. Phys.*, 51(25):253001, 2018.

[14] R. Iguchi and E. Saitoh. Measurement of spin pumping voltage separated from extrinsic microwave effects. *J. Phys. Soc. Japan.*, 86(1):011003, 2017.

[15] A. Azevedo, L. H. Vilela Leão, R. L. Rodríguez Suárez, A. F. L. Santos, and S. M. Rezende. Spin pumping and anisotropic magnetoresistance voltages in magnetic bilayers: Theory and experiment. *Phys. Rev. B*, 83(14):144402, 2011.

[16] J. C. Rojas Sánchez, N. Reyren, P. Laczkowski, W. Savero, J. P. Attané, C. Deranlot, M. Jamet, J. M. George, Laurent Vila, and H. Jaffrès. Spin pumping and inverse spin Hall effect in platinum: the essential role of spin-memory loss at metallic interfaces. *Phys. Rev. Lett.*, 112(10):106602, 2014.

[17] S. O. Valenzuela and M. Tinkham. Direct electronic measurement of the spin Hall effect. *Nature*, 442(7099):176–179, 2006.

[18] J. I. Ohe, A. Takeuchi, and G. Tatara. Charge current driven by spin dynamics in disordered Rashba spin-orbit system. *Phys. Rev. Lett.*, 99(26):266603, 2007.

[19] J. E. Gómez, B. Z. Tedlla, N. R. Álvarez, G. Alejandro, E. Goovaerts, and A. Butera. Spin transport parameters in $Ni_{80}Fe_{20}$/Ru and $Ni_{80}Fe_{20}$/Ta bilayers. *Phys. Rev. B*, 90(18):184401, 2014.

[20] K. Ando, S. Takahashi, J. Ieda, Y. Kajiwara, H. Nakayama, T. Yoshino, K. Harii, Y. Fujikawa, M. Matsuo, S. Maekawa, et al. Inverse spin-Hall effect induced by spin pumping in metallic system. *J. Appl. Phys.*, 109(10):103913, 2011.

[21] D. Velázquez Rodriguez, J. E. Gómez, L. Morbidel, P. A. Costanzo Caso, J. Milano, and A. Butera. High spin pumping efficiency in $Fe_{80}Co_{20}$/Ta bilayers. *J. Phys. D: Appl. Phys.*, 54(32):325002, 2021.

[22] M. A. W. Schoen, D. Thonig, M. L. Schneider, T. J. Silva, H. T. Nembach, O. Eriksson, O. Karis, and J. M. Shaw. Ultra-low magnetic damping of a metallic ferromagnet. *Nat. Phys*, 12(9):839–842, 2016.

[23] Y. Li, F. Zeng, S. S. L. Zhang, H. Shin, H. Saglam, V. Karakas, O. Ozatay, J. E. Pearson, O. G. Heinonen, Y. Wu, A. Hoffmann, W. Zhang. Giant anisotropy of Gilbert damping in epitaxial CoFe films. *Phys. Rev. Lett.*, 122(11):117203, 2019.

[24] J. E. Gómez, M. Guillén, A. Butera, and N. P. Albaugh. High performance electronic device for the measurement of the inverse spin Hall effect. *Rev. Sci. Instrum.*, 87(2):024705, 2016.

[25] D. Velázquez Rodriguez, J. E. Gómez, G. Alejandro, L. Avilés Félix, M. Vvan Landeghem, E. Goovaerts, and A. Butera. Relaxation mechanisms in ultra-low damping $Fe_{80}Co_{20}$ thin films. *J. Magn. Magn. Mater.*, 504:166692, 2020.

[26] J. M. D. Coey. *Magnetism and magnetic materials, 2^{nd} ed.* Cambridge University Press, 2010.

[27] T. L. Gilbert. A phenomenological theory of damping in ferromagnetic materials. *IEEE Trans. Magn.*, 40(6):3443–3449, 2004.

[28] J. Smit and H. G. Beljers. Philips res. *Rep*, 10(113):92, 1955.

[29] S. Martín Rio, A. Pomar, L. L. Balcells, B. Bozzo, C. Frontera, and B. Martínez. Temperature dependence of spin pumping and inverse spin Hall effect in permalloy/Pt bilayers. *J. Magn. Magn. Mater.*, 500:166319, 2020.

[30] M. Getzlaff. *Fundamentals of Magnetism*. Springer, 2008.

[31] J. Pelzl, R. Meckenstock, D. Spoddig, F. Schreiber, J. Pflaum, and Z. Frait. Spin-orbit-coupling effects on g-value and damping factor of the ferromagnetic resonance in Co and Fe films. *J. Condens. Matter Phys.*, 15(5):S451, 2003.

[32] R. Arias and D. L. Mills. Extrinsic contributions to the ferromagnetic resonance response of ultrathin films. *Phys. Rev. B*, 60(10):7395, 1999.

[33] M. J. Hurben and C. E. Patton. Theory of two magnon scattering microwave relaxation and ferromagnetic resonance linewidth in magnetic thin films. *J. Appl. Phys.*, 83(8):4344–4365, 1998.

[34] K. Zakeri, J. Lindner, I. Barsukov, R. Meckenstock, M. Farle, U. Von Hörsten, H. Wende, W. Keune, J. Rocker, S. S. Kalarickal, K. Lenz, W. Kuch, K. Baberschke, and Z. Frait. Spin dynamics in ferromagnets: Gilbert damping and two-magnon scattering. *Phys. Rev. B*, 76(10):104416, 2007.

[35] A. Butera, J. L. Weston, and J. A. Barnard. Ferromagnetic resonance of epitaxial $Fe_{81}Ga_{19}$ (110) thin films. *J. Magn. Magn. Mater.*, 284:17–25, 2004.

[36] J. R. Fermin, A. Azevedo, F. M. De Aguiar, B. Li, and S. M. Rezende. Ferromagnetic resonance linewidth and anisotropy dispersions in thin Fe films. *J. Appl. Phys.*, 85(10):7316–7320, 1999.

[37] A. Butera, J. Gómez, J. L. Weston, and J. A. Barnard. Growth and magnetic characterization of epitaxial $Fe_{81}Ga_{19}$/ MgO (100) thin films. *J. Appl. Phys.*, 98(3), 2005.

[38] J. Gómez and A. Butera. Ferromagnetic resonance line width in $Co_{(x)}$-$SiO_{2(1-x)}$ granular films.

Physica B Condens, 354(1-4):145–148, 2004.

[39] M. A. W. Schoen, J. M. Shaw, H. T. Nembach, M. Weiler, and T. J. Silva. Radiative damping in waveguide-based ferromagnetic resonance measured via analysis of perpendicular standing spin waves in sputtered permalloy films. *Phys. Rev. B*, 92(18):184417, 2015.

[40] L. Zhu, D. C. Ralph, and R. A. Buhrman. Effective spin-mixing conductance of heavy-metal-ferromagnet interfaces. *Phys. Rev. Lett.*, 123(5):057203, 2019.

[41] P. Deorani and Hy. Yang. Role of spin mixing conductance in spin pumping: Enhancement of spin pumping efficiency in Ta/Cu/Py structures. *Appl. Phys. Lett.*, 103(23):232408, 2013.

[42] M. Tokaç, S. A. Bunyaev, G. N. Kakazei, D. S. Schmool, D. Atkinson, and A. T. Hindmarch. Interfacial structure dependent spin mixing conductance in cobalt thin films. *Phys. Rev. Lett.*, 115(5):056601, 2015.

[43] S. Mankovsky, D. Ködderitzsch, G. Woltersdorf, and H. Ebert. First-principles calculation of the Gilbert damping parameter via the linear response formalism with application to magnetic transition metals and alloys. *Phys. Rev. B*, 87(1):014430, 2013.

[44] C. Guillemard, S. Petit-Watelot, S. Andrieu, and J. C. Rojas-Sánchez. Charge-spin current conversion in high quality epitaxial Fe/Pt systems: Isotropic spin Hall angle along different in-plane crystalline directions. *Appl. Phys. Lett.*, 113(26):262404, 2018.